Research article

Grigorios P. Zouros*, Georgios D. Kolezas, Evangelos Almpanis, Konstantinos Baskourelos, Tomasz P. Stefański and Kosmas L. Tsakmakidis*

Magnetic switching of Kerker scattering in spherical microresonators

https://doi.org/10.1515/nanoph-2020-0223
Received April 1, 2020; accepted June 12, 2020

Abstract: Magneto-optical materials have become a key tool in functional nanophotonics, mainly due to their ability to offer active tuning between two different operational states in subwavelength structures. In the long-wavelength limit, such states may be considered as the directional forward- and back-scattering operations, due to the interplay between magnetic and electric dipolar modes, which act as equivalent Huygens sources. In this work, on the basis of full-wave electrodynamic calculations based on a rigorous volume integral equation (VIE) method, we demonstrate the feasibility of obtaining magnetically-tunable directionality inversion in spherical microresonators (THz antennas) coated by magneto-optical materials. In particular, our analysis reveals that when a high-index dielectric is coated with a magneto-optical material, we can switch the back-scattering of the whole particle to forward-scattering simply by turning off/on an external magnetic field bias. The validity of our calculations is confirmed by reproducing the above two-state operation, predicted by the VIE, with full-wave finite-element commercial software. Our results are of interest for the design of state-of-the-art active metasurfaces and metalenses, as well as for functional nanophotonic structures, and scattering and nanoantennas engineering.

Keywords: active tuning; magneto-optical materials; scattering-directionality switching; spherical microresonators; THz regime.

***Corresponding authors: Grigorios P. Zouros**, Section of Condensed Matter Physics, National and Kapodistrian University of Athens, Panepistimioupolis, GR-157 84, Athens, Greece; School of Electrical and Computer Engineering, National Technical University of Athens, GR-157 73, Athens, Greece, E-mail: zouros@ieee.org; and **Kosmas L. Tsakmakidis**, Section of Condensed Matter Physics, National and Kapodistrian University of Athens, Panepistimioupolis, GR-157 84, Athens, Greece, E-mail: ktsakmakidis@phys.uoa.gr. https://orcid.org/0000-0003-4054-6086 (G.P. Zouros). https://orcid.org/0000-0003-2141-1338 (K.L. Tsakmakidis).
Georgios D. Kolezas: School of Electrical and Computer Engineering, National Technical University of Athens, GR-157 73, Athens, Greece, E-mail: geokolezas@central.ntua.gr. https://orcid.org/0000-0002-3888-5241
Evangelos Almpanis: Section of Condensed Matter Physics, National and Kapodistrian University of Athens, Panepistimioupolis, GR-157 84, Athens, Greece; Institute of Nanoscience and Nanotechnology, NCSR "Demokritos," Patriarchou Gregoriou and Neapoleos Street, Ag. Paraskevi, GR-153 10, Athens, Greece, E-mail: ealmpanis@gmail.com. https://orcid.org/0000-0001-8128-3118
Konstantinos Baskourelos: Section of Condensed Matter Physics, National and Kapodistrian University of Athens, Panepistimioupolis, GR-157 84, Athens, Greece, E-mail: konbask@phys.uoa.gr
Tomasz P. Stefański: Faculty of Electronics, Telecommunications and Informatics, Gdańsk University of Technology, ul. G. Narutowicza 11/12, 80-233, Gdańsk, Poland, E-mail: tomasz.stefanski@pg.edu.pl. https://orcid.org/0000-0002-3952-5731

1 Introduction

Following an increasing need for the deployment of active (tunable) photonic materials during recent years, magneto-optical-aided dielectric resonators have emerged as a valuable platform because of their unique and energy-efficient ability to control the propagation of optical waves. This is achieved through an external agent, mainly an external magnetic field, which alters the constitutive parameters of the magneto-optical material. Multi-fold enhancement of magneto-optical effects in Si nanodisks covered with thin nickel films, as well as in magneto-photonic array of nanodisks, has been experimentally demonstrated, for the development of active and nonreciprocal photonic nanostructures [1]. Magneto-optical materials have been successfully employed in cylindrical structures, such as infinite cylinders or arrays of such. In particular, their use was recently achieved in the context of active scattering, via the available Mie theory for infinite, two-dimensional circular gyroelectric/gyromagnetic cylinders whose solution can be separated into TE and TM modes [2]. Specifically, active control of directional scattering with a core–shell infinite cylinder driven by an

external magnetic field, as well as in cylindrical reconfigurable meta-lattices, has been theoretically examined by breaking the degeneracy of the multipoles in the subwavelength regime, thereby allowing the splitted modes to interfere and lead to directional optical switching [3, 4]. In addition, a normally irradiated array of magneto-optical core–shell cylinders has resulted in tunable anomalous back-scattering, where the extinction mean free path is longer than the transport mean free path [5].

Magneto-optical effects have been studied for attaining all-optical modulation [6], by exploiting nonlinear optical effects in two-dimensional materials, including graphene which involves magneto-optical effects in its conductivity model [7, 8], in magneto-optical active plasmonic resonators [9], in the implementation of highly tunable terahertz filters with magneto-optical Bragg gratings [10], in high-index structures where a Si spherical nanoantenna encapsulates a magneto-optical garnet core giving rise to magnetic and electric resonances that dominate the long-wavelength spectrum [11], in spatially dispersive gyrotropic semiconductor spheres [12], in obtaining topologically robust ultraslow waves in the presence of absorption and scattering channels [13], in laser devices for Q-switching [14], in nickel–silicon metasurfaces [15], nickel-based nanodisk arrays [16], and in photonic crystals with magnetized epsilon-near-zero metamaterials [17] for achieving magneto-optical response enhancement. Although high-index dielectrics do not exhibit the intrinsic losses of plasmonic materials, magneto-plasmonic media may offer additional functionalities, such as e.g. tunable plasmon-driven Hall currents existing in silver-coated Bi:YIG spherical scatterers [18].

The objective of our present work is to theoretically and numerically establish the feasibility of obtaining functional directionality inversion in spherical particles in the THz regime with the aid of magneto-optical materials that obey a Drude–Lorentz dispersive model. A straightforward strategy to achieve tunable forward- and back-scattering functionality is to deposit a magneto-optical layer on top of a high-index material. In this way, the high-index core contributes the magnetic dipolar mode, while the magneto-optical shell can exhibit the necessary electric dipolar plasmon that interferes with the magnetic dipolar mode, thereby leading to the desired directionality inversion. By employing a rigorous VIE method developed for the electromagnetic scattering by highly inhomogeneous gyroelectric spheres [19], and by means of full-wave electrodynamic calculations, we demonstrate such a tunable scattering-directionality inversion.

2 Methods

The setup of the subwavelength spherical antenna that will enable active directionality inversion is depicted in Figure 1. It consists of a high-index isotropic dielectric core of radius R_1 and permittivity ϵ_c, coated by a magneto-optical concentric shell of outer radius R_2. The magneto-optical material exhibits gyroelectric properties in the presence of an external DC magnetic field $B\hat{z}$, otherwise it is isotropic when the magnetic bias is null. The structure is embedded in free-space of permittivity ϵ_0 and permeability μ_0. The core and shell are nonmagnetic, i.e., their permeability is equal to μ_0. The configuration is illuminated by a plane electromagnetic wave impinging along the positive Oz semi-axis with its electric field being x-polarized.

A general way to describe the permittivity properties of the core–shell structure is by means of the inhomogeneous cartesian permittivity tensor

$$\bar{\bar{\epsilon}}(r) = \epsilon_0 \begin{bmatrix} \epsilon_1(r) & i\epsilon_2(r) & 0 \\ -i\epsilon_2(r) & \epsilon_1(r) & 0 \\ 0 & 0 & \epsilon_3(r) \end{bmatrix}, \quad 0 \leqslant r \leqslant R_2, \tag{1}$$

where r is the radial distance in the spherical coordinate system. Therefore, Eq. (1) comprises a two-branch function with $\epsilon_1(r) = \epsilon_3(r) \equiv \epsilon_{cr} = 16$ (ϵ_{cr} is core's relative permittivity) and $\epsilon_2(r) \equiv 0$, $0 \leqslant r \leqslant R_1$ for the isotropic core, while $\epsilon_1(r) \equiv 1 + [\omega_p^2(\omega_0^2 - \omega^2 - i\omega\gamma)]/[(\omega_0^2 - \omega^2 - i\gamma\omega)^2 - \omega^2\omega_c^2]$, $\epsilon_3(r) \equiv 1 + \omega_p^2/(\omega_0^2 - \omega^2 - i\gamma\omega)$ and $\epsilon_2(r) \equiv \omega_p^2\omega\omega_c/[(\omega_0^2 - \omega^2 - i\gamma\omega)^2 - \omega^2\omega_c^2]$, $R_1 < r \leqslant R_2$ for the magneto-optical shell. The relative permittivity elements of the shell obey a Drude–Lorentz dispersive model [20] with plasma angular frequency $\omega_p = 6\pi \times 10^{12}$ rad/s, resonance angular frequency $\omega_0 = 3\pi \times 10^{12}$ rad/s, cyclotron angular frequency $\omega_c = eB/m^*$ (e and m^* are the charge and effective mass of electrons), and damping angular frequency $\gamma = 0.06\pi \times 10^{12}$ rad/s [3]. Casting the permittivity of the structure in the form of Eq. (1), allows us to employ the VIE method, developed in [19], for the calculation of the scattering characteristics, i.e.,

$$\mathbf{E}(\mathbf{r}) = \mathbf{E}^{\text{inc}}(\mathbf{r}) + \left(k_b^2\mathbb{I} + \nabla\nabla^T\right) \int_{\mathbf{r}' \in V} g(\mathbf{r}, \mathbf{r}') \left[\frac{\bar{\bar{\epsilon}}(\mathbf{r}')}{\epsilon_0} - \mathbb{I}\right] \mathbf{E}(\mathbf{r}') \mathrm{d}\mathbf{r}'. \tag{2}$$

In Eq. (2), $\mathbf{E}^{\text{inc}}(\mathbf{r})$ is the incident electric field, k_b the background medium wavenumber—in our case the wavenumber of free space—$g(\mathbf{r}, \mathbf{r}')$ the free-space Green's function, and $\mathbb{I}$ the unity dyadic. The time factor $e^{-i\omega t}$

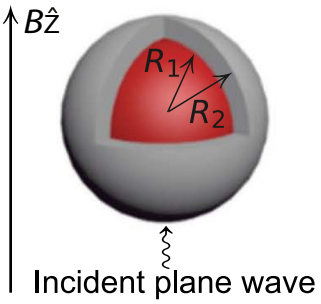

Figure 1: Schematic view of the spherical setup consisting of a high-index dielectric core (radius R_1) coated by a Drude–Lorentz magneto-optical shell (outer radius R_2). The external magnetic bias B is z-oriented, while the incoming plane wave impinges along the positive Oz semi-axis.

is assumed and suppressed throughout. For $\mathbf{r} \in V$, i.e., $r \leqslant R_2$, the electric field is written as an expansion of the form

$$\mathbf{E}(\mathbf{r}) = \sum_{m=-\infty}^{\infty} \sum_{n=|m|}^{\infty} \sum_{\ell=1}^{\infty} \left[\Gamma_{mn\ell} \mathbf{M}_{mn\ell}\left(k^M_{mn\ell}, \mathbf{r}\right) + \Delta_{mn\ell} \mathbf{N}_{mn\ell}\left(k^N_{mn\ell}, \mathbf{r}\right) + Z_{mn\ell} \mathbf{L}_{mn\ell}\left(k^L_{mn\ell}, \mathbf{r}\right) \right], \tag{3}$$

where $\mathbf{M}_{mn\ell}$, $\mathbf{N}_{mn\ell}$ and $\mathbf{L}_{mn\ell}$ are the Dini-type spherical vector wave functions (SVWFs) [19, 21], while $\Gamma_{mn\ell}$, $\Delta_{mn\ell}$ and $Z_{mn\ell}$ are unknown expansion coefficients. The values of the Dini-type wavenumbers $k^M_{mn\ell}$, $k^N_{mn\ell}$, $k^L_{mn\ell}$ are chosen as roots of proper eigenvalue equations [19], so that the vector sets $\mathbf{M}_{mn\ell}$, $\mathbf{N}_{mn\ell}$ are fully orthogonal in V and $\mathbf{L}_{mn\ell}$ decouples from $\mathbf{N}_{mn\ell}$. Following the procedure described in detail in [19] for the solution of Eq. (2), we finally arrive at the following expansion for the scattered field

$$\mathbf{E}^{\mathrm{sc}}(\mathbf{r}) = \sum_{m=-\infty}^{\infty} \sum_{n=|m|}^{\infty} D_{mn} \left[C^M_{mn} \mathbf{M}^{(3)}_{mn}(k_b, \mathbf{r}) + C^N_{mn} \mathbf{N}^{(3)}_{mn}(k_b, \mathbf{r}) \right], \tag{4}$$

where $\mathbf{M}^{(3)}_{mn}$ and $\mathbf{N}^{(3)}_{mn}$ are the SVWFs of the third kind and $D_{mn} = i^n [(2n+1)(n-m)!/n/(n+1)/(n+m)!]^{1/2}$. The scattering properties can then be expressed in terms of the computed scattering coefficients C^M_{mn}, C^N_{mn}, through the scattering cross section

$$Q_{\mathrm{sc}} = \frac{\lambda_b^2}{\pi} \sum_{m=-\infty}^{\infty} \sum_{n=|m|}^{\infty} \left(\left| C^M_{mn} \right|^2 + \left| C^N_{mn} \right|^2 \right), \tag{5}$$

where λ_b is the wavelength of the background medium, and through the asymmetry parameter [22]

$$g = \frac{\lambda_b^2}{\pi Q_{\mathrm{sc}}} \sum_{m=-\infty}^{\infty} \sum_{n=|m|}^{\infty} \mathrm{Re}\left\{ \left(C^M_{mn} \right)^* F_{mn} + \left(C^N_{mn} \right)^* G_{mn} \right\}. \tag{6}$$

In Eq. (6), Re denotes the real part, the asterisk complex conjugation, while $F_{mn} = P_{mn} C^N_{mn} + Q_{mn} C^M_{m,n+1} + R_{mn} C^M_{m,n-1}$, $G_{mn} = P_{mn} C^M_{mn} + Q_{mn} C^N_{m,n+1} + R_{mn} C^N_{m,n-1}$, with $P_{mn} = m/n/(n+1)$, $Q_{mn} = [n(n+2)(n-m+1)(n+m+1)/(n+1)^2/(2n+1)/(2n+3)]^{1/2}$ and $R_{mn} = [(n-1)(n+1)(n-m)(n+m)/n^2/(2n-1)/(2n+1)]^{1/2}$. It should be noted that the asymmetry parameter $g \in [-1, 1]$ can be employed for determining the scattering direction. In particular, if $g < 0$, more radiation is scattered in the backward direction, whereas $g > 0$ means that the scattering is directed more towards the forward direction. Therefore, examination of g through its sign change, reveals for which operational wavelength directionality inversion takes place. This will be made clear in the following Section.

3 Engineering functional spherical terahertz antennas for directionality inversion

The engineering of a setup for active directionality-inversion, is achievable by utilizing a magneto-optical material deposited on a high-index dielectric. Once the structure is manufactured, its geometrical parameters—i.e., radius R_2 and R_1/R_2 ratio—as well as its material, cannot be altered. Therefore, to realize functional directionality inversion, the application of an external agent—in the present case a magnetic bias—is necessary in order to alter the constitutive parameters of the coating and enable the switching between forward- and back-scattering. In the analysis that follows, we demonstrate a state which corresponds to forward-scattering in the absence of magnetic field, and to back-scattering with non-zero external magnetic bias.

Figure 2A depicts the normalized scattering cross section $Q_{\mathrm{sc}}/(\pi R_2^2)$ versus the normalized wavelength λ_b/R_2, under null magnetic field, for outer radius value $R_2 = 10$ μm, and $R_1/R_2 = 0.9$. In addition to the full-wave contribution to Q_{sc}—i.e., all spherical harmonics and angular momentum terms, required for convergence, contribute in Eq. (5)—the magnetic dipolar (MD) and electric dipolar (ED) terms (with the former and the latter being obtained solely from the contribution of $C^M_{1,1}$ and $C^N_{1,1}$, respectively), are also plotted. The resonant peak appearing at $\lambda_b/R_2 = 5.16$ corresponds to the higher order magnetic quadrupolar (MQ) term, whose sole contribution—through the C^M_{m2} expansion coefficient—is not depicted. The validity of our calculations is confirmed by comparison with HFSS commercial software. The blue dots depict results for $Q_{\mathrm{sc}}/(\pi R_2^2)$ obtained via HFSS simulations, thus establishing a good agreement with the VIE. It should be mentioned that an excellent agreement can be met, especially for the localized surface plasmon (LSP) appearing at $\lambda_b/R_2 = 9.92$, but it would require a tremendous amount of CPU time for HFSS to extract the spectrum using its finite element solver. In qualitative contrast to single high-index dielectric resonators where the first sub-wavelength resonance (as we move from higher to lower wavelengths) is the MD [23, 24], an extra resonance observed at $\lambda_b/R_2 = 9.92$ precedes the MD resonance at $\lambda_b/R_2 = 7.44$. This is due to the magneto-optical shell, whose dispersive properties change drastically around the plasma frequency. In particular, for frequencies below or equal to 3.353 THz (or, equivalently, for $\lambda_b/R_2 \geqslant 8.941$), the Drude–Lorentz dispersion exhibits plasmonic behavior, while, just above 3.353 THz, it yields near-zero permittivity values. The aforementioned plasmonic region is gray-shaded in Figure 2A. Therefore, the $\lambda_b/R_2 = 9.92$ peak corresponds to an LSP of a cavity-like hybrid of the shell [25, 26]. This is also confirmed by the near-field plot of the normalized magnitude $|\mathbf{E}|/\max(|\mathbf{E}|)$ of the total electric field on xz-plane which, as it is shown in Figure 2E, is concentrated within the plasmonic shell. We note here, that the LSP has a purely ED character, as confirmed by the green line in Figure 2A.

Figure 2B depicts the scattering-asymmetry parameter g in the same spectral window as in Figure 2A. With reference to the black curve—which corresponds to $B = 0$ T—three points in Figure 2A are of interest: point (I) at the intersection of MD–LSP resonances at $\lambda_b/R_2 = 8.93$ marked as (I), point (II) at the crossing of ED–MD resonances at $\lambda_b/R_2 = 6.6$, and the intermediate point (III) at

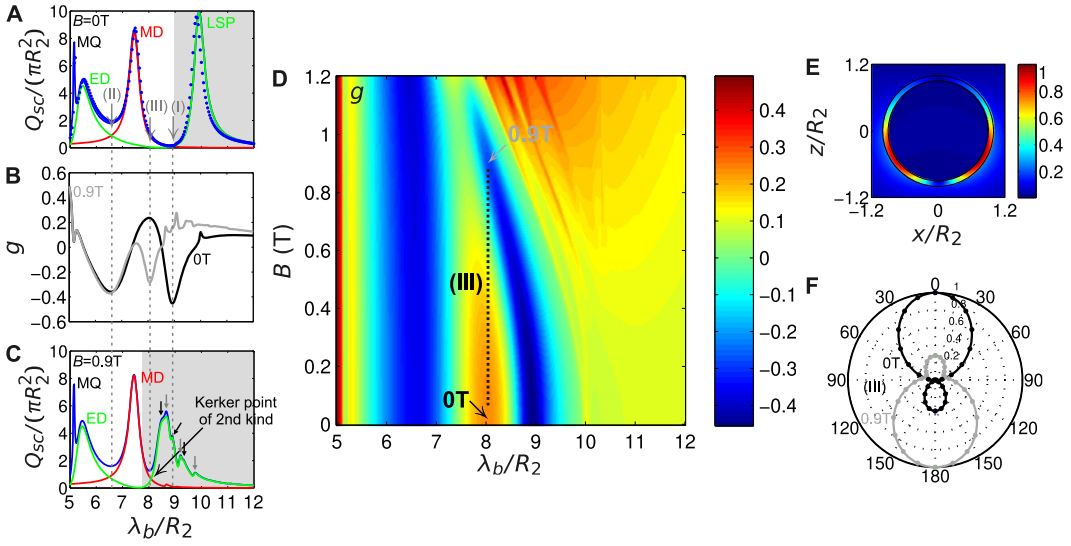

Figure 2: Scattering cross sections, asymmetry parameter, near field and polar (far field) plots to illustrate functional spherical antenna design for directionality inversion.

(A) Scattering cross section spectrum of a core–shell particle of total radius $R_2 = 10\,\mu m$, with core radius $R_1 = 0.9R_2$, under null external magnetic field. Blue curve: scattering cross section, i.e., including all terms of Eq. (5) up to a truncation order that ensures convergence; blue dots: scattering cross section via HFSS; red solid line: MD contribution to the scattering cross section; green solid line: ED contribution to the scattering cross section; point (I): Kerker point of second kind (back-scattering) at $\lambda_b/R_2 = 8.93$; point (II): Kerker point of second kind (back-scattering) at $\lambda_b/R_2 = 6.6$; point (III): Emerged forward-scattering point at $\lambda_b/R_2 = 8.04$. Gray region corresponds to wavelengths with plasmonic behavior of the shell material. (B) Scattering-asymmetry parameter within the given spectral window. Black: null magnetic field; gray: 0.9 T. (C) Scattering cross section spectrum for the same setup as in (A) but for external magnetic-field bias 0.9 T. Legends are the same as in (A). The small black/gray arrows indicate the mode splitting due to magnetic bias (see text). Black arrows: $m = -1$ non-degeneracy; gray arrows: $m = +1$ non-degeneracy. The large black arrow indicates the location of the Kerker point of second type which now, under 0.9 T magnetic field, coincides with point (III). Gray region corresponds to wavelengths with plasmonic behavior of the shell material. (D) Mapping of asymmetry parameter g versus B and λ_b/R_2. (E) Normalized magnitude $|\mathbf{E}|$ of the total electric field on xz-plane for the plasmonic resonance at $\lambda_b/R_2 = 9.92$ appearing in (A). (F) Polar/bistatic cross section (far field) for antenna operation at the preferential point $\lambda_b/R_2 = 8.04$. Black: forward-scattering at 0 T; gray: back-scattering at 0.9 T. Curves: VIE; dots: HFSS.

$\lambda_b/R_2 = 8.04$. The dipolar resonances within the spectral range up to $\lambda_b/R_2 = 8.9$ are typical subwavelength resonances that stem from the high-index dielectric core, where the intersections between the ED–MD and MD–LSP modes correspond to Kerker points of the second kind, as defined in [23]. We point out here that, for a single dielectric sphere [23], the first intersection—as we move from higher to lower wavelengths—corresponds to the Kerker point of the first kind where directional forward-scattering takes place, while, the second crossing, corresponds to the second Kerker point where strong back-scattering occurs. However, in our setup, due to the presence of an extra electrical dipolar mode, i.e., the LSP of the shell, there is an extra Kerker point of the second type, which is marked as (I) in Figure 2A. To further clarify this, we examine the behavior of the dominant dipolar terms $C_{1,1}^M$, $C_{1,1}^N$ versus λ_b/R_2. Both points (I), (II) satisfy the conditions $\mathrm{Im}(C_{1,1}^N) = -\mathrm{Im}(C_{1,1}^M)$ and $|C_{1,1}^N|^2 = |C_{1,1}^M|^2$ [23] that should hold for a point to be of the second Kerker type. These properties are interpreted as two local minima in g—in the absence of magnetic bias—precisely at points (I) and (II), as can be seen in Figure 2B. Interestingly, g yields one local maximum, indicating directional forward scattering, at an intermediate point marked as (III). Although in this emerged point, the condition $C_{1,1}^M = C_{1,1}^N$ [23] for Kerker points of the first kind, is now relaxed due to interference with the LSP, the resulted forward scattering is sufficient enough.

To further proceed in the design of active tuning, in Figure 2D we plot a two-dimensional mapping of g versus λ_b/R_2—in the same spectral range as in Figure 2A, B—and versus B, with values of the latter varying from zero to 1.2 T. Focusing on the value $\lambda_b/R_2 = 8.04$—point (III)—we observe a region around 1 T where g changes its positive sign and takes large negative values. The local minimum of negative g values is observed for $B = 0.9\,T$, as indicated by the arrow in Figure 2D. We then return to Figure 2B and plot g versus λ_b/R_2 for fixed $B = 0.9\,T$ (gray curve). This curve reveals a local minimum in the same position where $g(B = 0\,T)$ has its maximum. To elucidate the physics behind this mechanism, in Figure 2C we plot the scattering cross section spectrum for the same setup as in Figure 2A, but now for $B = 0.9\,T$. It is

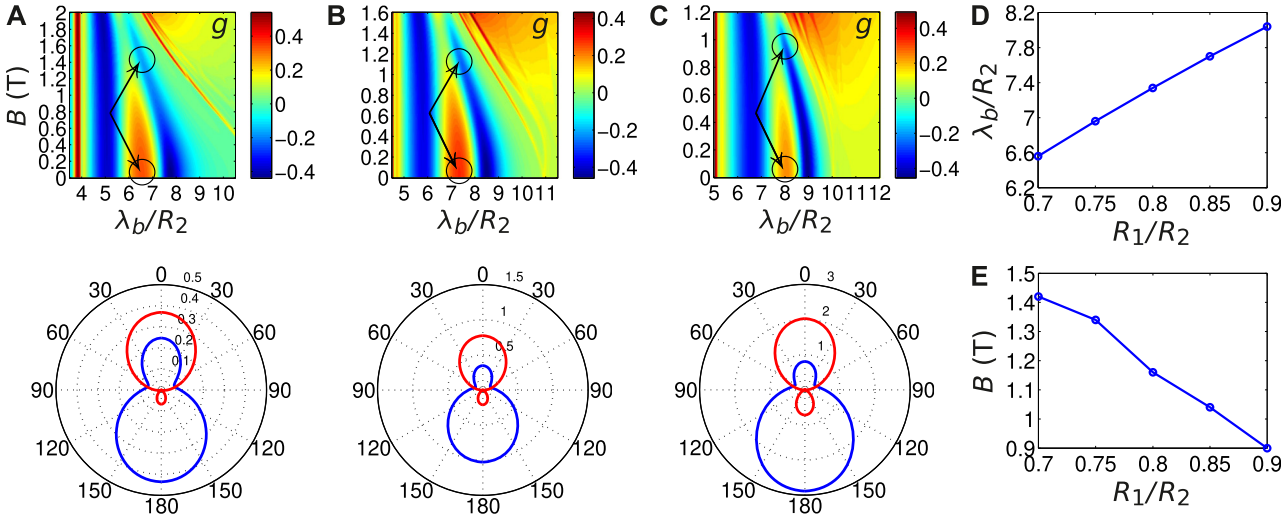

Figure 3: Scattering-assymetry maps and polar/bistatic scattering cross sections (far-field plots) for multiple setups with various R_1/R_2, when R_2 is fixed at 10 μm.
(A) $R_1/R_2 = 0.7$. Top: map of g. Bottom: $\sigma/(\pi R_2^2)$ at $\lambda_b/R_2 = 6.56$. Red: forward-scattering at 0 T; blue: back-scattering at 1.42 T. (B) $R_1/R_2 = 0.8$. Top: map of g. Bottom: $\sigma/(\pi R_2^2)$ at $\lambda_b/R_2 = 7.34$. Red: forward-scattering at 0 T; blue: back-scattering at 1.16 T. (C) $R_1/R_2 = 0.9$. Top: map of g. Bottom: $\sigma/(\pi R_2^2)$ at $\lambda_b/R_2 = 8.04$. Red: forward-scattering at 0 T; blue: back-scattering at 0.9 T. (D) Operational wavelength versus R_1/R_2 for which the setup supports active directionality inversion. (E) Values of B versus R_1/R_2 for achieving preferential back-scattering.

evident that now, the intersection between MD–LSP modes (Kerker point of second kind) moves to point (III), introducing a strong directional back-scattering at this wavelength. We point out here, that the LSP mode continuously shifts to lower wavelengths (from Figure 2A–C), by gradually increasing the external magnetic field from $B = 0$ to $B = 0.9$ T.

To better elucidate the optical response at the MD–LSP intersection in Figure 2C, as well as the spreading of its spectral shape where multiple peaks appear, we examine all terms that play a role in Eq. (5). Particularly, when magnetized, the sphere exhibits both uniaxial (birefringent) and gyrotropic optical response, as evident from Eq. (1) for $B \neq 0$. In Ref. [27] it is shown that uniaxial metallic particles mix the electric/magnetic character and multipole order (angular momentum index n) between the modes, followed by a respective $|m|$-degeneracy lifting. This is also valid for spherical resonators made from a birefringent material [28, 29]. Moreover, the gyrotropy induced by the external magnetic field further lifts the degeneracy between modes with index $\pm m$, resulting in an additional Zeeman-like splitting [30, 31]. However, in the present case, light couples only with the $m = \pm 1$ terms, since it impinges along the z axis [32]. The small black arrows indicate the location of the $m = -1$ resonances when obtained solely from the $C^N_{-1,1}$ term, while the small gray arrows correspond to $m = 1$ modes, as obtained from $C^N_{+1,1}$ the term. These C^N terms are sufficient for this analysis since the spectral features associated with the parent LSP mode preserve a predominant electric-dipolar character. With these in mind, we proceed by examining the possible combinations between predominantly-electric and -magnetic dipoles, respectively, i.e., $C^N_{+1,1}$–$C^M_{+1,1}$, $C^N_{-1,1}$–$C^M_{-1,1}$, $C^N_{+1,1}$–$C^M_{-1,1}$, and $C^N_{-1,1}$–$C^M_{+1,1}$. Each combination fulfills the Kerker condition of second kind in the proximity of point (III). Therefore, the strong back-scattering at $\lambda_b/R_2 = 8.04$, i.e., at the intersection between the two dipolar curves pointed out with the large black arrow in Figure 2C, is easily interpreted through a generalized (extension from the isotropic case) Kerker condition of the second kind.

In Figure 2F we plot the normalized (to unity) polar/bistatic (far field) scattering cross section $\sigma(\theta)$, $0 \leqslant \theta \leqslant 180°$, on yz-plane, when the spherical antenna operates at $\lambda_b/R_2 = 8.04$. Obviously, directionality inversion occurs through a switching of the external magnetic field from 0 to 0.9 T. Results from HFSS are plotted as dots in Figure 2F and fully coincide with the results obtained from VIE. This particular setup enables forward-scattering when the external bias is off, while when it is on, back-scattering occurs.

Next, the effect of R_1/R_2 ratio in the design of active tuning is studied in Figure 3. Each subfigure A, B, C examines the behavior of g and σ when R_1/R_2 takes the values 0.7, 0.8 and 0.9, respectively. The top subfigure in each case depicts the map of g versus λ_b/R_2 and B, while the bottom subfigure depicts the normalized $\sigma/(\pi R_2^2)$ when the

antenna operates at the respective to Figure 2 point (III). The spectral position of this point is also indicated by the black arrows/circles in each map of g. Judging from Figure 3A–C, in principle, directionality inversion can be achieved for various thin coating widths, nevertheless, the shell's thickness cannot be increased too much, otherwise the scattering response becomes nugatory, as it is evident from the $R_1/R_2 = 0.7$ case. In addition, the core–shell ratio has an impact on the frequency and external magnetic-field bias values for which the preferential operation is feasible. From the maps in Figure 3A–C it is evident that the location of point (III) shifts to lower frequencies and to lower magnetic-field magnitudes as R_1/R_2 increases. This behavior is summarized in Figure 3D, E which plot the precise values of λ_b/R_2 and B, for various core–shell ratios, for which directionality inversion takes place.

Focusing on the forward-scattering operation depicted by Figure 3A–C (bottom subfigures/red curves), when the R_1/R_2 ratio increases, the absolute value of the $\sigma(\theta = 0^\circ)$ point increases, but at the same time, the absolute value of the $\sigma(\theta = 180^\circ)$ point also increases. The same is true for the respective points at the back-scattering operation depicted by Figure 3A–C (bottom subfigures/blue curves). This behavior instructs us to perform an optimization of the setup versus R_1/R_2 in order to achieve an equal directionality for both operation states. To this end, we examine the variation of the relative forward-to-back ratio $\Lambda_f \equiv \sigma(0^\circ)/\sigma(180^\circ)$ versus R_1/R_2 during the forward-scattering operation, and the variation of the respective back-to-forward ratio $\Lambda_b \equiv \sigma(180^\circ)/\sigma(0^\circ)$, during the back-scattering operation. The results are depicted in Figure 4A. Obviously, Λ_f, Λ_b cannot be simultaneously maximized, however there exists the special value of $R_1/R_2 = 0.836$ for which $\Lambda_f = \Lambda_b$, thus achieving equal directionality for the forward- and back-scattering operations. This point corresponds to $\lambda_b/R_2 = 7.6$ while the back-scattering operation takes place for $B = 1.09$ T. In Figure 4B we plot the normalized $\sigma/(\pi R_2^2)$ when the antenna operates at this specific point. The directionality inversion is evident and an excellent agreement with HFSS is met.

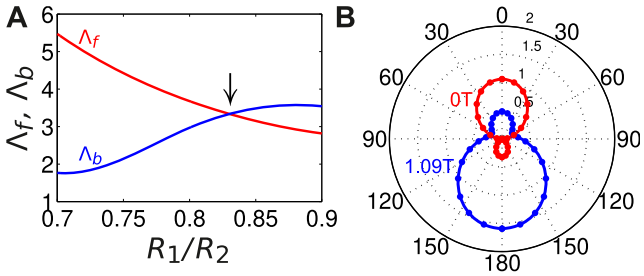

Figure 4: Optimization of the setup versus R_1/R_2, while $R_2 = 10$ μm, in both forward- and back-scattering operation to achieve equal directionality.
(A) Ratios Λ_f, Λ_b versus R_1/R_2 for which the setup supports active directionality inversion. Red: Λ_f; blue: Λ_b. The black arrow indicates the value $R_1/R_2 = 0.836$ where $\Lambda_f = \Lambda_b$. This point corresponds to $\lambda_b/R_2 = 7.6$ and $B = 1.09$ T. (B) $\sigma/(\pi R_2^2)$ at $\lambda_b/R_2 = 7.6$. Red: forward-scattering at 0 T; blue: back-scattering at 1.09 T. Curves: VIE; dots: HFSS.

Next we calculate the working bandwidth for our setup. For the designed device with $R_1/R_2 = 0.9$, from Figure 4A we deduce that $\Lambda_f = 2.8$ and $\Lambda_b = 3.5$ when directionality inversion occurs. We therefore seek in Figure 2D a common range Δf in the dark-red ($B = 0$ T) and in the dark-blue ($B = 0.9$ T) region of point (III), for which Λ_f and Λ_b maintain the same aforementioned levels. This yields a working bandwidth of $\Delta f \approx 27$ GHz around $\lambda_b/R_2 = 8.04$ (corresponding to an operation frequency of 3.73 THz). We have verified that for all frequencies inside this range, directionality inversion indeed takes place, with far-field plots similar to the one in Figure 2F. To complement this study, we further examine how the working bandwidth is affected by R_1/R_2. Focusing on the range from $R_1/R_2 = 0.8$ to 0.9, Δf is maintained at the same level of 27 GHz for all ratios, but interestingly, it can be enhanced at the optimized point $R_1/R_2 = 0.836$ of Figure 4A, where the latter yields $\Delta f \approx 41$ GHz.

Up to this point, the setup is stimulated by a plane wave which impinges parallel to the orientation of the external magnetic field. In Figure 5 we examine how the switching performance is affected due to a relative orientation between $\mathbf{E}^{\text{inc}}(\mathbf{r})$ and $B\hat{z}$, when the former impinges with an angle θ_0 with respect to the Oz semi-axis, while keeping $R_1/R_2 = 0.9$. To this end, the asymmetry parameter g needs to be computed under oblique incidence. To achieve this goal, we consider the primed coordinate system $x'y'z'$ that is rotated with respect to the original coordinate system xyz, so that $\mathbf{E}^{\text{inc}}(\mathbf{r}')$ remains x-polarized and propagates parallel to the z'-axis. Then, by applying appropriate transformation formulas for the SVWFs [33], we obtain the expression of $\mathbf{E}^{\text{sc}}(\mathbf{r}')$ in the rotated frame and proceed to compute g as given by Eq. (2). In Figure 5A we plot the scattering cross section ratios Λ_f, Λ_b versus incidence angle θ_0. Independently from θ_0, Λ_f is constant since when $B = 0$ T, the coating is isotropic and the incidence orientation does not affect g. Contrariwise, Λ_b can reach a minimum and a maximum value at $\theta_0 = 30^\circ$ and $\theta_0 = 90^\circ$, respectively. The corresponding bistatic scattering cross sections are depicted in Figure 5C, D. From the bistatic scattering cross section plots we deduce that, for the given configuration, when $0^\circ \leqslant \theta_0 < 30^\circ$, the forward-scattering point $\sigma(\theta_0)$ when $B = 0$ T, is always smaller than the back-scattering point $\sigma(180^\circ - \theta_0)$ when $B \neq 0$ T. This can be confirmed by Figure 3C (bottom subfigure) where $\theta_0 = 0^\circ$, but also from other $\sigma/(\pi R_2^2)$, $\theta_0 < 30^\circ$

plots that have been computed and not given here. On the contrary, when $\theta_0 \gtrsim 30^\circ$, $\sigma(\theta_0)|_{B=0\,\mathrm{T}}$ overpasses $\sigma(180^\circ - \theta_0)|_{B\neq 0\,\mathrm{T}}$. This is evident from Figure 5C, D where, at the limiting case where Λ_b reaches its minimum—i.e., at $\theta_0 = 30^\circ$—$\sigma(\theta_0)|_{B=0\,\mathrm{T}} \equiv \sigma(180^\circ - \theta_0)|_{B=0.86\,\mathrm{T}}$, while at $\theta_0 = 90^\circ$, $\sigma(\theta_0)|_{B=0\,\mathrm{T}} > \sigma(180^\circ - \theta_0)|_{B=0.83\,\mathrm{T}}$. It should be noted that at oblique incidence, although the main lobe in the forward-scattering pattern points precisely at the θ_0-direction, the back-scattering pattern has a tilt with respect to the $(180^\circ - \theta_0)$-direction. This can be observed from the $\theta_0 = 30^\circ$ case in Figure 5C where a 15° tilt exists in the back-scattering direction, making the main lobe of the far-field pattern to point at 165°, rather than 150°. Finally, Figure 5B depicts the values of B needed for achieving preferential back-scattering at the prescribed angles θ_0. As we shift from parallel to normal orientation between the incident wavevector and $B\hat{z}$, the B values should be slightly decreased. In addition, $\lambda_b/R_2 = 8.04$ for all θ_0 since when $B = 0$ T, the oblique incidence does not affect the asymmetry parameter g.

In Figure 6 we plot the near-fields and in particular the normalized magnitude $|\mathbf{E}|/\max(|\mathbf{E}|)$ of the total electric field on yz-plane. The field patterns in Figure 6 correspond to the $R_1/R_2 = 0.9$ ratio antenna when the latter operates at the preferential point $\lambda_b/R_2 = 8.04$ under forward-scattering (Figure 6A) and back-scattering (Figure 6B) activity. The forward- and back-propagation in the two states can be clearly seen from field distribution in the background free-space medium. Figure 6C, D are zoom-in versions of A, B, respectively. The field pattern inside the sphere in Figure 6C is indicative of a MD resonance, although point (III) in Figure 2A does not precisely correspond to the MD resonance at $\lambda_b/R_2 = 7.44$. Contrariwise, the field pattern in Figure 6D is more complicated owing to the gyroelectric nature of shell's permittivity due to the external magnetic field. This yields a strongly localized field inside the shell, but inside the core the similarity of the pattern to a MD resonance is evident.

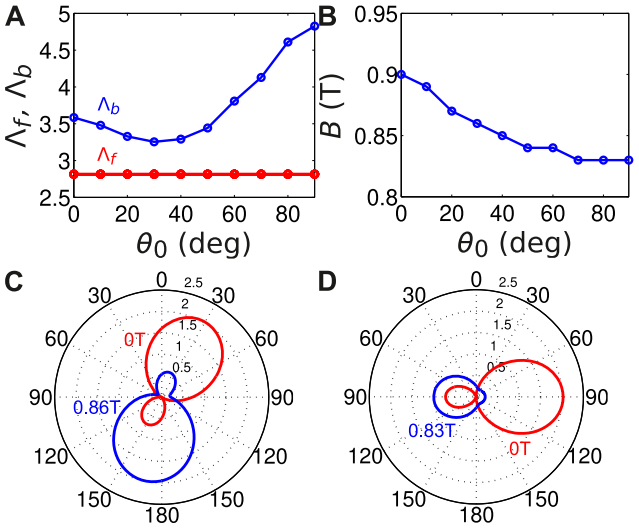

Figure 5: Study of the switching performance under oblique incidence of the impinging plane wave for $R_1/R_2 = 0.9$, while $R_2 = 10\,\mu$m and $\lambda_b/R_2 = 8.04$. The external magnetic field is always z-directed.
(A) Ratios Λ_f, Λ_b versus θ_0. Red: Λ_f; blue: Λ_b. (B) Values of B versus θ_0 for achieving preferential back-scattering. (C) $\sigma/(\pi R_2^2)$ at $\theta_0 = 30^\circ$. Red: forward-scattering at 0 T; blue: back-scattering at 0.86 T. (D) $\sigma/(\pi R_2^2)$ at $\theta_0 = 90^\circ$. Red: forward-scattering at 0 T; blue: back-scattering at 0.83 T.

4 Scalability to the nano regime

Recently, it was experimentally demonstrated that static magnetic field-assisted resonant topological cavities, provide a platform for the implementation of photonic waveguides in the quantum regime [34]. In addition, it was theoretically and experimentally observed that graphene-based inhomogeneous strains can induce pseudomagnetic effects in the optical regime that are similar to the magnetic effects produced by the magneto-optical devices in the THz regime [35]. In particular, such effective magnetic fields can reach thousands of Tesla, exceeding standard laboratory values [36]. As a consequence, this would also increase the

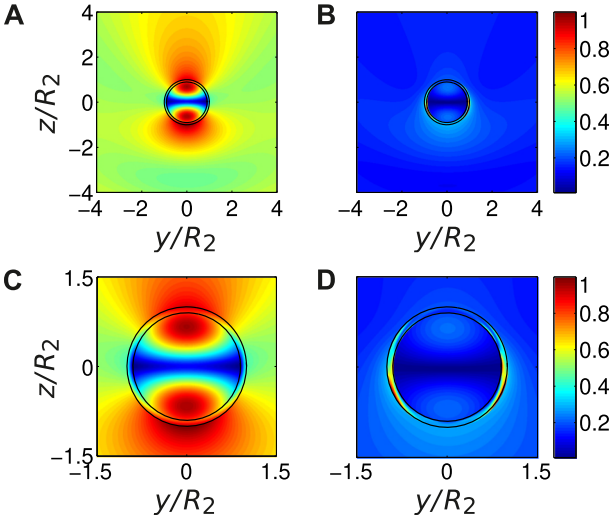

Figure 6: Near-field images of the normalized magnitude $|\mathbf{E}|$ of the total electric field on yz-plane. The values of parameters are the same with the ones in Figure 3C and the antenna is stimulated at $\lambda_b/R_2 = 8.04$.
(A) Forward-scattering operation at 0 T. (B) Back-scattering operation at 0.9 T. (C) Zoom-in plot at 0 T. (D) Zoom-in plot at 0.9 T.

working bandwidth of the proposed device at the nanoscale, since the latter is linearly dependent on the magnetic field [20]. This rescaling observation led us to apply our analytical model in the THz regime, and export various intrinsic properties being scalable to shorter wavelengths.

5 Conclusion

In summary, we have shown that by judiciously designing a high-index spherical microresonator coated by an active magneto-optical material, full directionality inversion can be achieved. Based on analytical calculations and corroborating full-wave electrodynamic simulations, we have shown that by actively tuning the constitutive parameters of the magneto-optical coating by means of an external magnetic bias, tunable forward- and back-scattering functionality occurs. Our design is based on a Drude–Lorentz dispersive coating operating above its plasma frequency. The permittivity properties of the magneto-optic material change from those of an isotropic material, in the absence of magnetic field, to those of a gyroelectric one when the magnetic field is applied. Our results may allow the flexible and with low energy cost active switching of emerging metasurface and metalenses devices for applications like beam steering [37], as well as tunable nanophotonic structures such as magneto-metasurface devices for one-way transmission and sensing [38], or functional metamaterials like magneto-optical core–shell-based composed metamaterial devices for optical memory control [39].

Acknowledgement: G.P.Z., E.A., K.B., and K.L.T. were supported by the General Secretariat for Research and Technology (GSRT) and the Hellenic Foundation for Research and Innovation (HFRI) under Grant No. 1819.
Research funding: This work was supported by Hellenic Foundation for Research and Innovation (HFRI), General Secretariat for Research and Technology (GSRT) (No. 1819).

References

[1] M. G. Barsukova, A. S. Shorokhov, A. I. Musorin, D. N. Neshev, Y. S. Kivshar, and A. A. Fedyanin, "Magneto-optical response enhanced by Mie resonances in nanoantennas," *ACS Photon.*, vol. 4, pp. 2390–2395, 2017.
[2] J. C. Palais, "Scattering from a gyrotropic cylinder," *IEEE Trans. Antennas Propag.*, vol. 11, pp. 505–506, 1963.
[3] M. Q. Liu, C. Y. Zhao, and B. X. Wang, "Active tuning of directional scattering by combining magneto-optical effects and multipolar interferences," *Nanoscale*, vol. 10, pp. 18282–18290, 2018.
[4] M. Q. Liu and C. Y. Zhao, "Reconfigurable metalattices: combining multipolar lattice resonances and magnetooptical effect in far and near fields," *J. Appl. Phys.*, vol. 126, p. 113105, 2019.
[5] T. J. Arruda, A. S. Martinez, and F. A. Pinheiro, "Electromagnetic energy and negative asymmetry parameters in coated magneto-optical cylinders: applications to tunable light transport in disordered systems," *Phys. Rev. A*, vol. 94, p. 033825, 2016.
[6] H. Chen, C. Wang, H. Ouyang, Y. Song, and T. Jiang, "All-optical modulation with 2D layered materials: status and prospects," *Nanophotonics*, Published online ahead of print, 20190493, 2020.
[7] D. A. Kuzmin, I. V. Bychkov, V. G. Shavrov, and V. V. Temnov, "Plasmonics of magnetic and topological graphene-based nanostructures," *Nanophotonics*, vol. 7, pp. 597–611, 2018.
[8] J. W. You, S. R. Bongu, Q. Bao, and N. C. Panoiu, "Nonlinear optical properties and applications of 2D materials: theoretical and experimental aspects," *Nanophotonics*, vol. 8, pp. 63–97, 2019.
[9] E. Atmatzakis, N. Papasimakis, V. Fedotov, G. Vienne, and N. I. Zheludev, "Magneto-optical response in bimetallic metamaterials," *Nanophotonics*, vol. 7, pp. 199–206, 2018.
[10] B. Hu, Y. Zhang, and Q. J. Wang, "Surface magneto plasmons and their applications in the infrared frequencies," *Nanophotonics*, vol. 4, pp. 383–396, 2015.
[11] N. de Sousa, L. S. Froufe-Pérez, J. J. Sáenz, and A. García-Martín, "Magneto-optical activity in high index dielectric nanoantennas," *Sci. Rep.*, vol. 6, p. 30803, 2016.
[12] T. Dong and X. Ma, "Electromagnetic scattering by gyrotropic semiconductor spheres when considering spatial dispersion," *J. Phys. D: Appl. Phys.*, vol. 51, p. 285302, 2018.
[13] K. L. Tsakmakidis, O. Hess, R. W. Boyd, and X. Zhang, "Ultraslow waves on the nanoscale," *Science*, vol. 358, p. eaan5196, 2017.
[14] T. Goto, R. Morimoto, J. W. Pritchard, et al., "Magneto-optical Q-switching using magnetic garnet film with micromagnetic domains," *Opt. Express*, vol. 24, pp. 17635–17643, 2016.
[15] M. G. Barsukova, A. I. Musorin, A. S. Shorokhov, and A. A. Fedyanin, "Enhanced magneto-optical effects in hybrid Ni–Si metasurfaces," *APL Photon.*, vol. 4, p. 016102, 2019.
[16] F. Freire-Fernández, M. Kataja, and S. van Dijken, "Surface-plasmon-polariton-driven narrow-linewidth magneto-optics in Ni nanodisk arrays," *Nanophotonics*, vol. 9, pp. 113–121, 2020.
[17] Z. Guo, F. Wu, C. Xue, et al., "Significant enhancement of magneto-optical effect in one-dimensional photonic crystals with a magnetized epsilon-near-zero defect," *J. Appl. Phys.*, vol. 124, p. 103104, 2018.
[18] P. Varytis and N. Stefanou, "Plasmon-driven large Hall photon currents in light scattering by a core–shell magnetoplasmonic nanosphere," *J. Opt. Soc. Am. B*, vol. 33, pp. 1286–1290, 2016.
[19] G. P. Zouros and G. C. Kokkorakis, "Electromagnetic scattering by an inhomogeneous gyroelectric sphere using volume integral equation and orthogonal Dini-type basis functions," *IEEE Trans. Antennas Propag.*, vol. 63, pp. 2665–2676, 2015.
[20] K. L. Tsakmakidis, L. Shen, S. A. Schulz, et al., "Breaking Lorentz reciprocity to overcome the time-bandwidth limit in physics and engineering," *Science*, vol. 356, pp. 1260–1264, 2017.
[21] W. C. Chew, *Waves and Fields in Inhomogeneous Media*. New York: Van Nostrand Reinhold, 1990.

[22] C. F. Bohren and D. R. Huffman, *Absorption and Scattering of Light by Small Particles*. New York: Wiley, 1983.
[23] J. M. Geffrin, B. García-Cámara, R. Gómez-Medina, et al., "Magnetic and electric coherence in forward- and back-scattered electromagnetic waves by a single dielectric subwavelength sphere," *Nat. Commun.*, vol. 3, p. 1171, 2012.
[24] G. D. Kolezas, G. P. Zouros, and K. L. Tsakmakidis, "Engineering subwavelength nanoantennas in the visible by employing resonant anisotropic nanospheroids," *IEEE J. Sel. Top. Quantum Electron.*, vol. 25, p. 4700912, 2019.
[25] C. Tserkezis, G. Gantzounis, and N. Stefanou, "Collective plasmonic modes in ordered assemblies of metallic nanoshells," *J. Phys. Condens. Mater.*, vol. 20, p. 075232, 2008.
[26] C. S. Levin, C. Hofmann, T. A. Ali, et al., "Magnetic-plasmonic core-shell nanoparticles," *ACS Nano*, vol. 3, pp. 1379–1388, 2009.
[27] G. Gantzounis, "Plasmon modes of axisymmetric metallic nanoparticles: a group theory analysis," *J. Phys. Chem. C*, vol. 113, pp. 21560–21565, 2009.
[28] G. P. Zouros, "Eigenfrequencies and modal analysis of uniaxial, biaxial, and gyroelectric spherical cavities," *IEEE Trans. Microw. Theory Technol.*, vol. 65, pp. 20–27, 2017.
[29] G. P. Zouros, "Analysis of multilayered gyroelectric spherical cavities by weak form VIE formulation," *IEEE Trans. Microw. Theory Technol.*, vol. 65, pp. 4029–4036, 2017.
[30] E. Almpanis, "Dielectric magnetic microparticles as photomagnonic cavities: enhancing the modulation of near-infrared light by spin waves," *Phys. Rev. B*, vol. 97, p. 184406, 2018.
[31] E. Almpanis, G. P. Zouros, P. A. Pantazopoulos, K. L. Tsakmakidis, N. Papanikolaou, and N. Stefanou, "Spherical optomagnonic microresonators: triple-resonant photon transitions between Zeeman-split Mie modes," *Phys. Rev. B*, vol. 101, p. 054412, 2020.
[32] J. A. Stratton, *Electromagnetic Theory*. New York: McGraw-Hill, 1941.
[33] L. Tsang, J. A. Kong, and R. T. Shin, "Radiative transfer theory for active remote sensing of a layer of nonspherical particles," *Radio Sci.*, vol. 19, pp. 629–642, 1984.
[34] B. Bahari, A. Ndao, F. Vallini, A. E. Amili, Y. Fainman, and B. Kanté, "Nonreciprocal lasing in topological cavities of arbitrary geometries," *Science*, vol. 358, pp. 636–640, 2017.
[35] M. C. Rechtsman, J. M. Zeuner, A. Tünnermann, S. Nolte, M. Segev, and A. Szameit, "Strain-induced pseudomagnetic field and photonic Landau levels in dielectric structures," *Nat. Photon.*, vol. 7, pp. 153–158, 2013.
[36] T. Ozawa, H. M. Price, A. Amo, et al., "Topological photonics," *Rev. Mod. Phys.*, vol. 91, p. 015006, 2019.
[37] W. Liu and A. E. Miroshnichenko, "Beam steering with dielectric metalattices," *ACS Photon.*, vol. 98, pp. 1733–1741, 2018.
[38] S. Chen, F. Fan, X. He, M. Chen, and S. Chang, "Multifunctional magneto-metasurface for terahertz one-way transmission and magnetic field sensing," *Appl. Opt.*, vol. 54, pp. 9177–9182, 2015.
[39] T. J. Arruda, A. S. Martinez, and F. A. Pinheiro, "Controlling optical memory effects in disordered media with coated metamaterials," *Phys. Rev. A*, vol. 98, p. 043855, 2018.